AN IMAGE ANALYSIS METHOD TO MEASURE CROSS-SECTIONAL TRACHEID DIMENSIONS ON SOFTWOOD INCREMENT CORES

Mattias Moëll

Ph.D. Candidate

and

Gunilla Borgefors

Professor,
Center for Image Analysis, Lägerhyddv. 17,
752 37 Uppsala, Sweden

ABSTRACT

Anatomical properties of wood affect the properties of wood products. In this paper, an automated image analysis method for measuring cross-sectional tracheid dimensions of softwood cores is presented. The images used were single slice, confocal reflected light microscope images. By the use of the proposed method, automatic measurements of radial and tangential lumen diameter, as well as radial cell-wall thickness, of almost all individual tracheids are obtainable.

Keywords: Image analysis, confocal microscopy, shape-based thresholding, distance transform, Hough transform, skeletonization, tracheid measurements.

INTRODUCTION

Picea abies (L.) Karst and *Pinus sylvestris* L. are the two dominant tree species in Sweden, and the wood of these species is used to produce timber as well as pulp and paper products. Figure 1 shows a confocal tandem reflected light microscope image of tracheids. Different morphological characteristics of the tracheids, which can be measured on cross sections of wood, significantly affect the properties of wood products (Kibblewhite 1980, 1999).

Automated or almost automated methods to measure tracheid dimensions improve the possibilities for wood research, since manual measurements are too time-consuming for larger numbers of measurements.

Substantial research concerning the use of image analysis for wood anatomy analysis has been carried out. However, the use of image analysis combined with high resolution, i.e., high magnification, microscopy of increment cores has not been sufficiently investigated. The high magnification makes it possible not only to measure individual radial and tangential lumen diameter, but also the radial cell-wall thickness for individual cells. We present an automatic method to obtain these measures in transverse cross sections of wood using images such as Fig. 1.

Related research

Confocal microscope images provide both improved image quality and improved image contrast compared to conventional transmitted light microscope images for cross-sectional wood images (Donaldson and Lausberg 1998).

Hougardy (1976) reviewed the early image analysis instrumentation for microscope image analysis and also gave an overview of the basic steps in automatic image analysis. Many of the earlier image analysis methods are mentioned, and the usefulness of image analysis in wood anatomy and dendrochronology is stated in Jagels and Telewski (1990).

McMillin (1982) illustrated how geometrical features of tracheid shapes can be obtained manually in a binarized image. The video im-
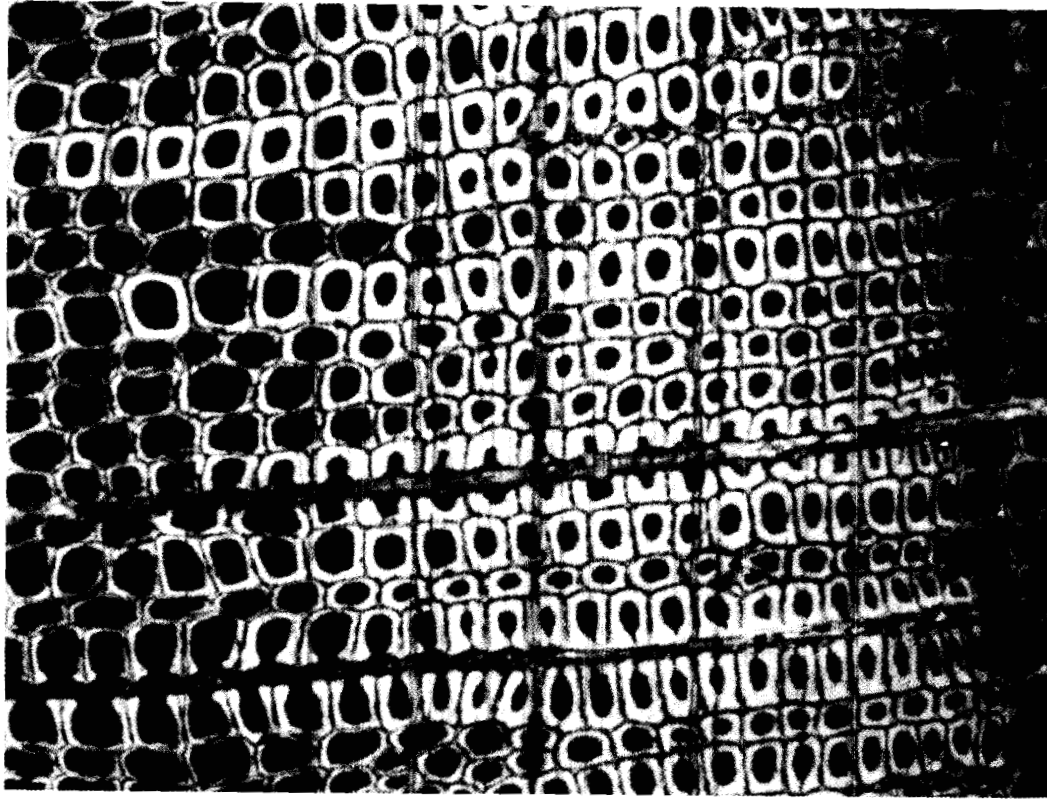
Fig. 1. "Typical" transverse section of Scots pine (*Pinus silvestris* L.).

age processor of Ilic and Hillis (1983) handled geometric measurements on binary images, but also gave the option of the operator's manually outlining the tracheids to be measured. Needing less computer power than earlier, the boundary and area of binary lumen objects were also obtained in Telewski et al. (1983). Using a "circularity index," Jagels and Dyer (1983) studied the shape of the lumen; the circumference of the lumen was traced manually. In Lee and Rosen (1985), the use of object analysis and object boundary tracing of binary images of tracheids was further investigated.

Classification based on gray-level values was used in Yanosky and Robinove (1986), mainly to study environmental effects on wood anatomy. Here, improved resolution was mentioned as likely to improve results.

Using a commercial image analyzer, sample preparation methods for measurements of cell-wall proportion were tested in Schnell and Sell (1989). A slight underdetection of cell walls was noted, and the importance of good contrast images was pointed out. A tesselation approximating the tracheid cell-wall boundaries was obtained using a weighted distance transform in Peachey and Osborne (1990). Here, the method is dependent upon manual thresholding and other manual operations.

The use of image analysis as a tool to measure wood density was investigated in Clauson and Wilson (1991), where the assumption is made that an optical property, i.e., the intensity value when converting a video color image to a gray-level image, is proportional to wood density. Instead of the optical property assumption, the use of morphological measurements, i.e., the ratio of cell-wall area to total area, was investigated as a measure of wood density in Park and Telewski (1993).

Using image analysis on low resolution images, in combination with X-ray densitometry,

the Silviscan system, described in Evans (1994) and Evans et al. (1995), measures radial and tangential cell diameter, and wood density. From these measures other parameters, such as tracheid wall thickness, are calculated.

Another tool that has proved very useful for studying cross-sectional images of wood is the two-dimensional Fast Fourier Transform (FFT). In Fujita et al. (1996), the FFT was performed on dot maps of hardwood vessels, i.e., slightly increased central points of the vessels, and the FFT power spectral patterns were visually inspected for wood classification purposes. The FFT of dot maps and of net maps, i.e., maps where the cell walls have been reduced to lines, were used to study tracheid arrangements in Diao et al. (1996). With the use of the FFT, individual measurements are not obtainable. Instead averages over the image are obtained directly.

Several geometric indices were used to characterize morphological properties of hardwood vessels in Diao et al. (1997) and cross-sectional tracheid shapes for softwoods in Diao et al. (1999). Difficulties in measuring tracheids near ray cells were noted.

High-resolution imaging and image analysis were used to perform microscopic analysis and microtensile testing of wood fibers in Schaler et al. (1996).

Cross-sectional measurements of pulp fibers were obtained using confocal microscopy and image analysis in Jang et al. (1992) and Chan et al. (1998).

IMAGE ACQUISITION

The sample preparation and image aquisition using a confocal tandem reflected light microscope (TSM 4448 Noran Instruments, Wisconsin, USA) are described in Hannrup et al. (1999). The illumination source was a 200-W quicksilver lamp. No staining was used, and no emission filters were used. These images as well as an early version of our image processing system, were used for forest research by Hannrup et al. (1999) and Pape et al. (1999). The images were 640 × 480 pixels using 8-bit gray-levels, and the image resolution was 0.864 μm/pixel. Gray-level 0 corresponds to black and 255 to white.

In general, the measurement accuracy of an image analysis system is dependent on the quality of the images input to the system. Using the preparation techniques and confocal laser scanning microscopy as in Donaldson and Lausberg (1998) would improve the results even more.

The hardware used for image analysis was a DEC Alpha Station.

Image analysis

Tracheid features and method overview

In Fig. 1 a transverse section of wood is shown. This image will be used as a running example to illustrate the various steps in the image analysis method. The dominating features of Fig. 1 are the brighter cell walls and the darker lumina. Two rays in the image run horizontally through the whole image. The radial direction in the image is the direction of the cell files, and the tangential direction is perpendicular to the radial direction.

The aim is to correctly measure the radial and tangential lumen diameter, and radial cell-wall thickness, for as many of the cells in the image as possible. Since we are interested in averages over many cells for various tree samples and for various times within each tree (different annual rings), it does not matter if a few cells are missed or mismeasured, as long as this does not affect the averages much, i.e., if the errors are not systematic, favoring or removing some particular cell size. Post-processing of the data is performed to further reduce the effect of mismeasurements.

To measure lumen diameters, the lumina are separated from the rest of the image using a shape-based thresholding method. The cell-wall boundaries are then approximated by the skeleton of the complement of the lumen image. The image is rotated so that the cell file direction, i.e. radial direction, corresponds to the horizontal image direction. This is done

automatically by using a Hough transform to find the rotation angle. It is then feasible to merely count pixels in the horizontal and the vertical directions of the image to measure the cells.

The thresholded image may contain objects other than lumina, such as parts of ray cells or parts of middle lamellae due to overlapping of the gray-level distributions of the different features. Therefore, the procedure also includes classification of objects in order to increase the number of correctly identified lumen objects.

Segmentation of cell lumen

Segmentation is nearly always the most crucial part of image analysis. In this section, the image analysis procedure for separating the cell lumen from the rest of the image is presented. The procedure consists of three parts.

1. Thresholding; creates a binary image containing the cell lumen.
2. Watershed segmentation; identifies individual objects (lumina) in the binary image, by splitting some of the objects consisting of more than one lumen.
3. Object classification into lumen or non-lumen objects.

Thresholding.—The difficulties of thresholding, or segmentation, are often overlooked in the literature, where in many cases manually, subjectively, chosen thresholds are used.

The gray-levels for lumen, middle lamellae, and resin canals are generally darker than the cell walls. There is also a variation of the gray-levels within objects. A ray may, depending on where it has been cut, be both dark and bright. Keeping this in mind, it is clear that no threshold gives a perfect segmentation. There is a tradeoff between achieving a set with all lumen pixels included *and* achieving a set where few non-lumen objects are included.

A thresholding operation with threshold T converts the gray-level image $p(x,y)$ into a binary image with the foreground S_1 (white) and the background S_0 (black).
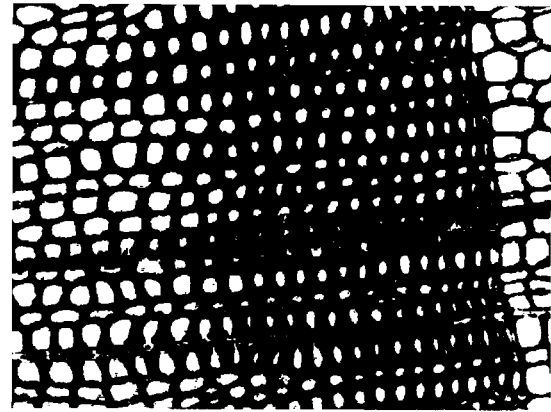
Fig. 2. Threshold region of Fig. 1, $T = 61$. The threshold region is white.

$$S_0(T) = \{(x, y): p(x, y) > T\},$$

$$S_1(T) = \{(x, y): p(x, y) \leq T\} \qquad (1)$$

The threshold is automatically set using the P^2/A histogram thresholding method according to Ranefall et al. (1998). This has been illustrated in detail for this type of images in Moëll and Borgefors (1998). The optimal threshold of Fig. 1 is found to be $T_{P2A} = 61$. The binary image is shown in Fig. 2.

Watershed segmentation.—After thresholding, the set $S_1(T)$ consists of a number of isolated objects, most of which are a single lumen. However, some objects are clusters of lumina or lumina connected to part of a ray cell, etc.

To label objects and to split the connected objects, a watershed algorithm is used (Orbert et al. 1993; Vincent and Soille 1991). The watershed algorithm splits objects that consist of roundish "blobs" connected by narrow "bridges," i.e., some earlywood cells in the right of Fig. 2. The aim is that most of the objects after the watershed segmentation should correspond to a single lumen in the original image. The watershed algorithm is based on the (3,4)-distance transform (Borgefors 1986). In this application, it was found suitable to split objects when the width of the bridge was less than 20% of the maximal distance from a pixel in the object to the back-

ground, i.e., the maximal radius of the object. Using 20%, or a similar low value, most objects consisting of more than one lumen, but only a few objects consisting of only one lumen, are split.

An image, here called the watershed image, is thus created where each separate object is assigned an unique integer value, a label.

Classification using size and shape.—Using measures of size and shape, the objects of the watershed image will be classified as either lumen or non-lumen. For each of the objects in the watershed image the *area*, defined as the number of pixels in the object, is calculated together with the p^2/a value, defined as:

$$\frac{p^2}{a} = \frac{(\text{object perimeter})^2}{4\pi \text{ area}}, \qquad (2)$$

where the object perimeter is obtained by eight-connectivity contour tracing and weighting diagonal steps with $\sqrt{2}$.

By deleting objects not having $12 \leq area \leq 2500$, most of the middle lamellae (<12) and resin canal objects (>2500) are deleted. Deleting objects not having $0.2 \leq p^2/a \leq 2.5$ will remove most of the objects that consist of more than a single lumen. The area thresholds, which of course are dependent on the scale, must not be too restrictive, as the variation in the size of the lumina is considerable. In the continuous case, $p^2/a \geq 1$, but due to digitization much lower values can occur, especially for small objects. The sensitivity of the p^2/a thresholds is not high, since most non-lumen objects have a p^2/a value far from 1.0. Even though the tracheid shape is species-dependent, the interval $0.2 \leq p^2/a \leq 2.5$ is broad enough to be used for both *Picea abies* and *Pinus sylvestris*.

The center of mass, (x_c, y_c) for an object is defined as:

$$x_c = \sum_{i=1}^{N_o} \frac{x_i}{\text{area}}, \qquad y_c = \sum_{i=1}^{N_o} \frac{y_i}{\text{area}} \qquad (3)$$

where N_o is the number of pixels in the object and (x_i, y_i) are the coordinates of a pixel in the object. All objects with their center of mass

outside of the object are deleted, since these clearly do not correspond to lumina. All objects touching the image border are also deleted, since they cannot be satisfactorily measured.

Depending on image quality, segmentation may in some cases lead to some parts of the same ray cell being segmented as cell wall and other parts as lumen. For such images, the classification using size and shape of objects is least efficient. Therefore, a second classification will be carried out, classifying objects as ray objects or not (see section on Detection of rays).

Image rotation using the hierarchial Hough transform

In most images the cell files are ordered, i.e., separate cell files are ordered as parallel lines. For the actual cell measurements, it is an advantage if the cell files are oriented along the horizontal axis. Therefore, the dominant angle of the cell files relative to the horizontal axis is calculated.

To determine the angle, i.e., the equation of a straight line fitted to the lumen mass centers, the line-detecting Hough transform (Gonzalez and Woods 1992) can be used. The line equation is

$$\rho = x \cos \theta + y \sin \theta, \qquad (4)$$

where ρ is the distance to the origin and θ is the angle to the horizontal.

Note that we are interested here in the angle for a *set* of parallel lines (cell files), not the lines as such. We use the hierarchial line-detecting Hough transform of Yu and Jain (1996). The dominant angle is determined in two steps, a coarse one and a fine one. The mass centers, using the definition of Eq. (3), of the remaining objects, which should be almost exclusively lumina, were used as input points to the Hough transformation. To get more data, and also to minimize the effect of digitization, the eight neighboring pixels of the mass centers were also used as input points.

The reader is referred to Yu and Jain (1996) for the method. However, it contains many pa-
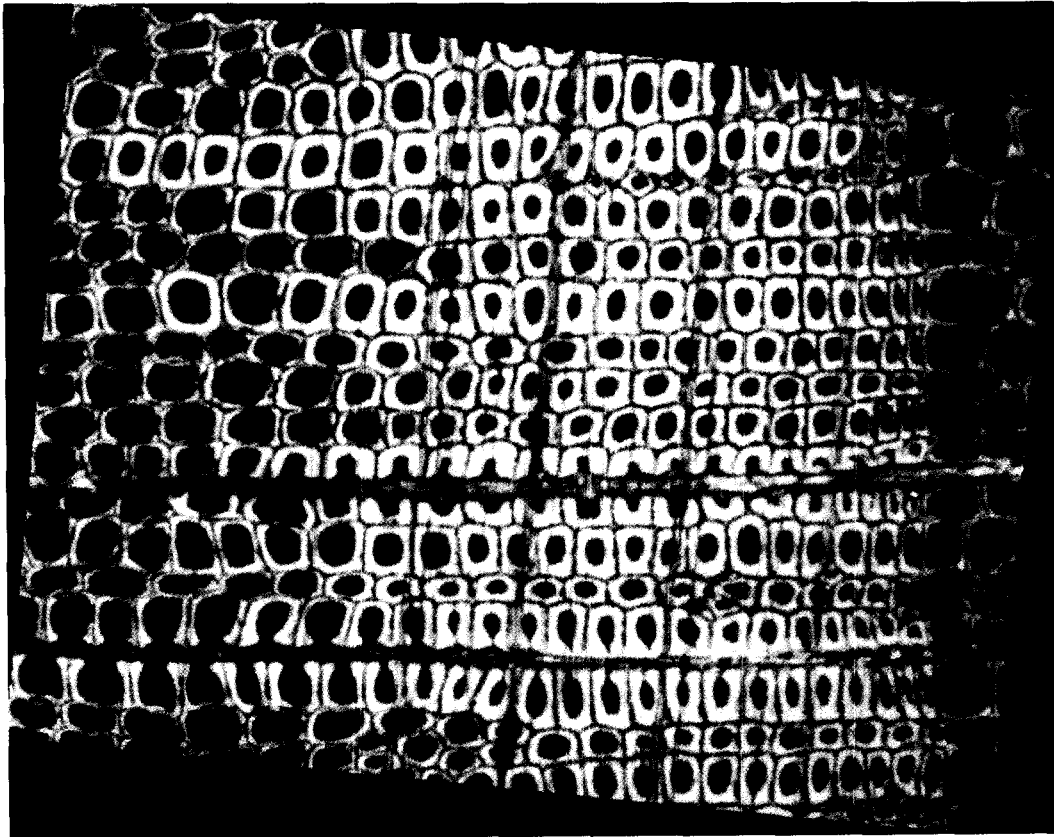
FIG. 3.   The rotated image of Fig. 1. Cell files are horizontal.

rameters that must be fine-tuned for our applications. The values we finally used were the following:

For coarse detection, $\theta = \theta_1$, we have angular resolution $\delta\theta_1 = 1°$, polar distance resolution $\delta\rho = 2$ pixels, range $\Delta\theta_1 = [-90°, +90°]$, and the two-dimensional window was $\theta_1 \in [\theta_{1m} - 5°, \theta_{1m} + 5°]$ with no boundaries on the polar distance ρ, where θ_{1m} denotes the angle of the accumulator cell with the maximum value.

The weighted average of the angles of the accumulator cells, which have values larger than half of the maximum accumulator cell value, is denoted $\hat\theta_1$.

The parameters during fine detection, $\theta = \theta_1$, were angular resolution $\delta\theta_0 = 0.25°$, polar distance resolution $\delta\rho = 2$ pixels, range $[\hat\theta_1 - 5\delta\theta_1, \hat\theta_1 + 5\delta\theta_1] = [\hat\theta_1 - 5°, \hat\theta_1 + 5°]$, and the

two-dimensional window $\theta_0 \in [\hat\theta_1 - 5°, \hat\theta_1 + 5°]$, with no boundaries on ρ.

The weighted average of the angles of the accumulator cells, which have values larger than half of the maximum accumulator cell value, in the fine detection two-dimensional window is denoted $\hat\theta_0$. This is the final estimate of the dominant angle.

Rotating the gray-level image by the Hough angle, $\hat\theta_0$, the cell files become oriented along the horizontal direction. The advantage of rotating the gray-level image instead of the labelled object image is that this introduces fewer discretization errors. When rotating the gray-level image, we use bilinear interpolation (Gonzalez and Woods 1992). The rotated image of Fig. 1 is found in Fig. 3.

In the rotated gray-level image, pixels not corresponding to a pixel in the unrotated orig-

inal image will get gray-level value 0. These pixels, here called the rotation border pixels, become a black border around the rotated image (see Fig. 3). To be able to distinguish between the rotation border pixels and the rest of the rotated image, all 0-valued pixels in the unrotated original image (there are very few) were set to 1 prior to rotation. Only the black border pixels in the rotated image thus have the value 0.

The rotated image is thresholded from 1 to T_{P2A}, and watershed and classification using size and shape are now carried out for the rotated image. To remove from the rotated image objects that were image border objects in the original image, the image border objects in the original image were rotated and their centers of mass, in the rotated image, calculated. Objects in the rotated image that enclosed such a mass center were deleted.

Detection of rays

As mentioned in the Section Segmentation of cell lumen, depending on image quality, size and shape classification might not be enough to classify rays correctly. In this section, a method for detecting pixel rows running through the most distinctive rays is described. Such rays will have the greatest effect on the measurements. The main concern is to reduce the number of objects wrongly classified as lumen, rather than to correctly identify each single ray.

In most cases, rays have a low variation in gray-level and are likely to have fewer object pixels, i.e., pixels with gray level less than or equal to T_{P2A}, than the cell files directly above or below. A pixel row is thus classified as being part of a ray if it has a low gray-level variation and contains a low number of object pixels.

In images with no rays, there were few cases where rows were wrongly classified as part of a ray. By classifying objects that intersect pixel rows classified as rays as ray objects, and deleting these objects, the remaining objects are more likely to be lumen objects. In Fig. 3,
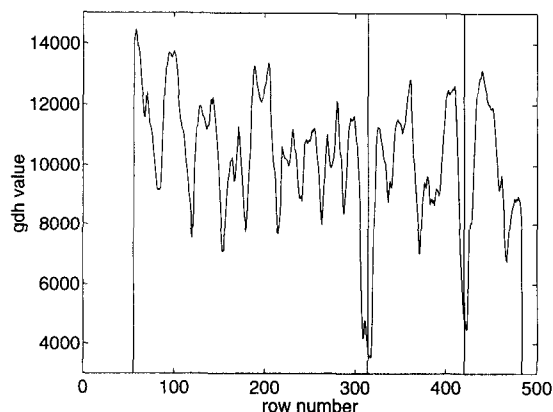
FIG. 4. Gray-level difference histogram of Fig. 3.

one pixel row in the upper ray and two pixel rows in the lower ray will be classified as rays.

The ray detection will be performed only for pixel rows where the number of nonzero pixels is greater than 80% of the total number of pixels. This to prevent the border, introduced by the image rotation, to interfere (see Section Image rotation using the hierarchical Hough transform).

The variation of gray-levels is measured by calculating the sum of the absolute difference of the gray-levels for all consecutive pixel pairs on that row. Computing this sum and dividing by the number of nonzero pixels in the row, gives a histogram here called the gray-level difference histogram, $gdh[y]$. Thus

$$gdh[y] = \frac{\sum_{x=1}^{N_x} |g(p(x, y)) - g(p(x - 1, y))|}{N_y^{>0}},$$

$$\text{for each row } y, \text{ with } \frac{N_y^{>0}}{N_x} > 0.80$$

(5)

where N_x and $N_y^{>0}$ denote the number of pixels and nonzero pixels on row y, respectively. Figure 4 shows the gray-level difference histogram of Fig. 3. In Fig. 4, the rows at $y = 314$ and $y = 420$ have been marked, since by visual inspection it is seen that they correspond to the approximate middle of the two rays in Fig. 3.

As a selective classification parameter to measure how significantly low the gray-level variation is, a parameter called global min depth, *Gmd* is used. To achieve a robust classification parameter, the global minimum of the gray-level difference histogram was compared to the minimum of a number of weighted averages of the local minima. The global min depth is defined as the minimum of the difference between the global minimum, min_y $gdh(y)$, and the weighted averages $\bar{w}_1$, $\bar{w}_2$, $\bar{w}_3$ and $\bar{w}_4$ of the local minima in the histogram,

$$Gmd = \min_{j=1,2,3,4} \left[\bar{w}_j - \min_y gdh(y) \right], \quad (6)$$

where the weight for the local minima *k* when calculating the weighted average $\bar{w}_j$ was:

$\bar{w}_1$: all weights $w_{1k} = 1$ (7)

$\bar{w}_2$: the weight w_{2k}, for the local minimum *k*, is the difference between the nearest local maximum to the right and the local minimum   (8)

$\bar{w}_3$: the weight w_{3k}, for the local minimum *k*, is the difference between the nearest local maximum to the left and the local minimum   (9)

$\bar{w}_4$: the weight w_{4k}, for the local minimum *k*, is $w_{2k} + w_{3k}$.   (10)

For the image in Fig. 3, the averages were $\bar{w}_1$ = 9453, $\bar{w}_2$ = 7541, $\bar{w}_3$ = 7837, and $\bar{w}_4$ = 7684.

The criteron for classifying a pixel row as having significantly low gray-level variation is:

$$gdh[y] \le \min_y gdh(y) + f1 \times Gmd. \quad (11)$$

If Eq. (11) is true, then row *y* is classified as having significantly low gray-level variation. The value of the control parameter *f*1 times the global min depth is a measure on how much larger than the global min that $gdh[y]$ may be, in order for row *y* to be classified as having significantly low gray-level variation.

Counting the number of object pixels for each pixel row yields a histogram, here called the row threshold histogram, $rth[y]$:

$rth[y]$ = the number of nonzero pixels on row *y* with gray-level $\le T_{P2A}$

for each row, *y*, with
$N_y^{>0}/N_x > 0.80$ (12)

The $rth[y]$ value for pixel row, *y*, can be seen as the object density for that pixel row. Both rows *y* = 314 and *y* = 420, which by visual inspection are seen to correspond to rays in the image of Fig. 3, correspond to deep minima in $rth[y]$, i.e., have few object pixels.

A deep local minimum in the row threshold histogram is likely to be a pixel row not corresponding to the lumen part of a cell file, and thus be more likely to be part of a ray. A criterion for classifying pixel rows as not belonging to the lumen part of a cell file is:

$rth[y]$ < *f*2 × average of all local mininima in *rth*,   (13)

If Eq. (13) is true, then pixel row *y* is classified as not corresponding to the lumen part of a cell file. This criterion does not distinguish between if a pixel row contains few object pixels because it is part of the cell-wall part of the cell file, or if it is part of the middle lamella, or if it is part of ray. There is no need for such a distinction, since the objective of criteria Eq. (13) is to reduce the possibility of the lumen part of the cell file being classified as part of a ray, and thus avoiding deletion of unnecessarily many correctly identified lumen objects.

In this application, the control parameters were set for pine and spruce to $f1_{pine}$ = 0.30, $f1_{spruce}$ = 0.53, and *f*2 = 1.1 for both species. The control parameters were tuned by choosing, from an increment core, images with varying appearance of ray cells and changing the parameters so that most of the rays, and no false rays, were detected.

Since the gray-levels vary within an object, a lumen might contain pixels with gray-levels higher than the T_{P2A}, and an object classified as a lumen thus might contain holes. By applying a 4 × 4 ringfilter (see Fig. 5) to the

p_1	p_2	p_3	p_4
p_{12}	q_1	q_2	p_5
p_{11}	q_4	q_3	p_6
p_{10}	p_9	p_8	p_7

Fig. 5. The mask of the 4 × 4 ring filter.

labelled and classified lumen image, holes can be filled, while the object edges are preserved.

When all pixels p_i, $i = 1, \ldots , 12$ have the same label > 0, the pixels q_j, $j = 1, \ldots , 4$ are set to that label. Otherwise, the values of q_j remain the same.

Measurements

The measurements carried out on the objects classified as lumina are radial lumen diameter, tangential lumen diameter, and radial cell-wall thickness. The radial lumen diameter is measured as the sum of the distances from the center of mass to the left and right object borders in the horizontal direction. The sum of distances from the center of mass to the upper and lower object borders in the vertical direction is the tangential lumen diameter.

To approximate the tracheid boundaries, and thus to be able to measure the radial cell-wall thickness, the skeleton of the complement region of the thresholding region is used. For the rotated image, the thresholding region is the pixels $p(x,y)$ such that $1 \leq p(x, y) \leq T_{P2A}$. The complement of this region is all pixels $p(x, y) > T_{P2A}$. Not including the rotation border pixels (value 0) in the set where the skeleton is calculated gives a slightly better tracheid boundary approximation near the rotation border. Note that no lumen classification

was performed, i.e., no objects were removed from the threshold region, before the complement operation, only thresholding. The skeleton was calculated using the method in Sanniti di Baja (1994). It is based on the (3,4) distance transform, which is also used in the watershed algorithm. The skeleton is beautified, i.e., the skeleton jaggedness is reduced, and the branches are pruned, i.e., certain protrusions/ branches are removed, as described in Sanniti di Baja (1994). Branch pruning removed spurious branches in the lumina. We used the value 5 for the branch-pruning parameter, which means that "bumps" of the tracheid walls up to 5 pixles thick are disregarded.

Figure 6 shows the skeleton and the objects remaining after classification using size and shape, and ray detection. As seen in Fig. 6, in the horizontal direction, the skeleton separates the cell wall between two individual tracheids well, i.e., a good tracheid boundary approximation is obtained. The radial cell-wall thickness is calculated as the average of the distances from the left object (lumen) border to the skeleton and the right object border to the skeleton. The distances are measured in the horizontal direction on the pixel row passing through the center of mass.

Although the number of misclassified, and thus mismeasured, objects has been reduced, some misclassified objects may still be present. To minimize even further the effect of such objects on the averages, a priori knowledge of cell wall and lumen shape is used to post-process the data. Data from objects where the cell wall on one side is more than twice as large as on the other side are discarded. Also, data for objects where one horizontal, or vertical, lumen radius is more than twice as large as the other one are discarded.

Figure 7 shows the final lumen and cell-wall measurements. The contrast and brightness have been altered compared to Figs. 1 and 3, to improve the visualization of the measurements. In Fig. 7, only two objects have wrongly been classified as lumina (see the lower ray, left and middle). Some lumina that did not fol-
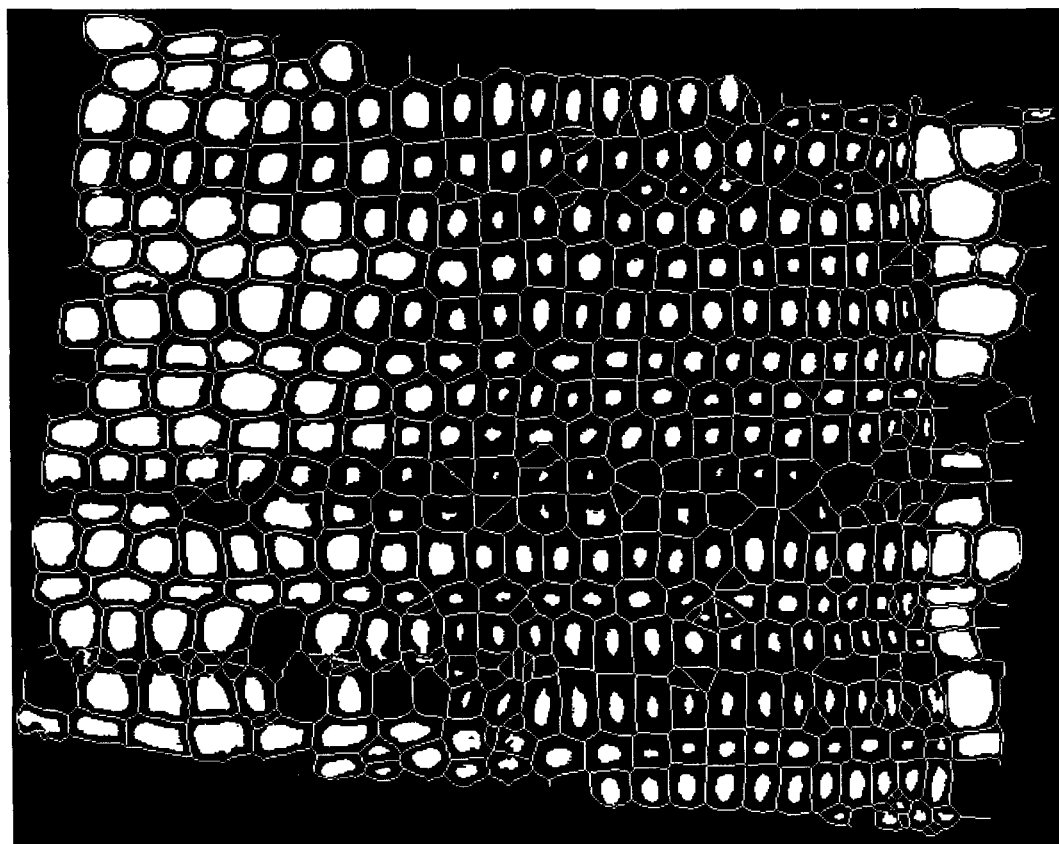
FIG. 6.   The skeleton and the remaining objects.

low the classification criteria have also been removed, but as can be seen, they are not many. Most missed lumina occur at the right edge of the image, where the cell walls are very dark (see Fig. 1), and thus the thresholding fails.

For forest research, averages in the radial direction are desirable, and a radial window, with size depending on the application, may be set. Inside the radial window, the individual measurements are averaged. Figure 8 shows the mean values when using a radial window size of 25 pixels (approximately 22 μm).

If one would like to further reduce the effect of the misclassified objects, individual cells could be compared to the averages and outliers removed.

CONCLUSIONS

In this paper, we have introduced an image analysis method for tracheid measurements on confocal images of softwood increment cores. In forest research, where a great many samples are to be studied, automation is necessary for reducing operator bias, as well as for reducing the time required to acquire data. Although the proposed method contains several thresholds, such as the watershed bridge, object size and shape, and ray detection control parameters, it is sufficient, in spite of the inhomogenous properties of the biological material wood, to tune these parameters using only a few images of the increment core. By choosing appropriate images, i.e., earlywood/latewood transitions, images with different size and appear-
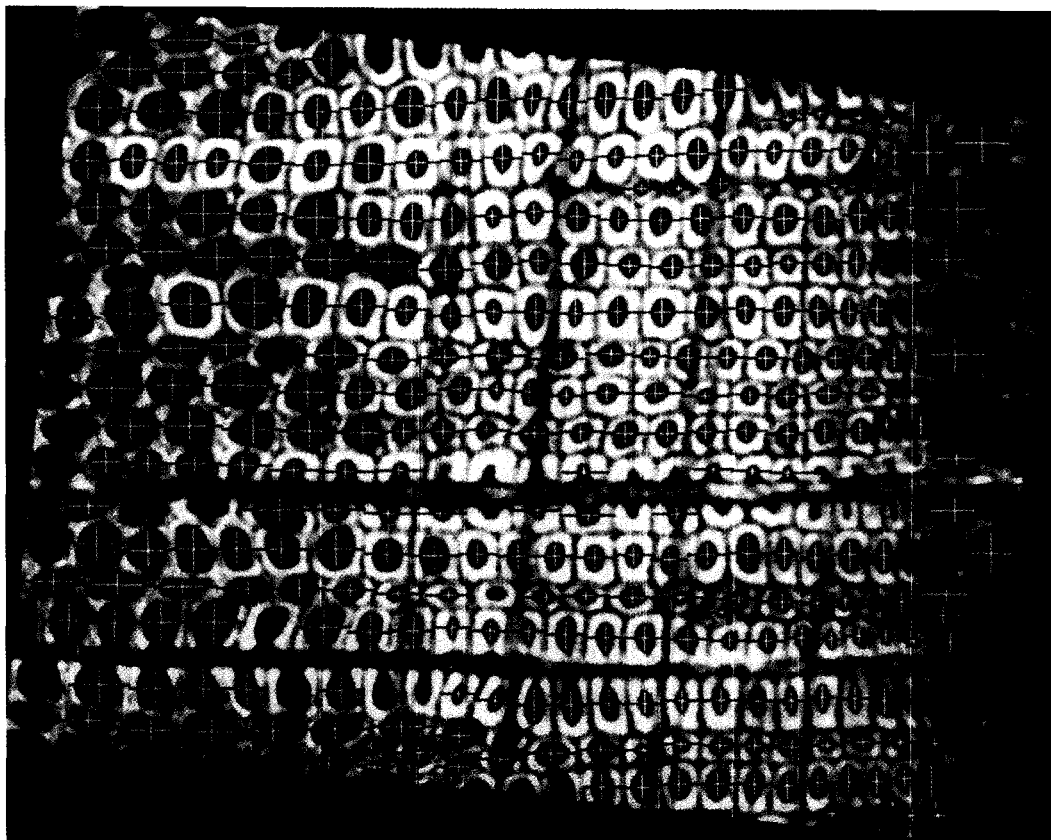
FIG. 7.   Lumen (white lines) and cell-wall (black lines) measurements after post-processing.

ance of resin canals and rays, for parameter tuning, the same parameters could be used for different increment cores of the same species. Because of the anatomical differences of different softwood species, however, the parameters should be tuned separately for separate species.

Since an increment core may contain poor resolution images, manual inspection should be used to confirm the automatic thresholding. Also manual inspection should identify images containing wood with distortions, i.e., wood that does not feature the radial ordering of cell files, for example juvenile wood, compression wood, etc., since in such images radial or tangential directions are hardly identifiable even with the human eye.

A detailed investigation into performance of the system, as well as a comparison with man-

ual measurements, will be presented in the future.

FIG. 8.   Lumen and cell-wall average values in Fig. 7, using a 25 pixel window.

REFERENCES

BORGEFORS, G. 1986. Distance transformations in digital images. Computer Vision, Graphics and Image Processing 34:344–371.

CHAN, B. K., H. F. JANG, AND R. S. SETH. 1998. Measurement of fibre wall thickness by confocal microscopy and image analysis. Appita 51(3):229.

CLAUSON, M. L., AND J. B. WILSON. 1991. Comparison of video and X-ray for scanning wood density. Forest Prod. J. 41(3):58–62.

DIAO, X., T. FURUNO, AND T. UEHARA. 1996. Analysis of cell arrangements in softwoods using two-dimensional fast Fourier Transform. Mokuzai Gakkaishi 42(7):634–641.

————, ————, AND ————. 1997. Quantitative morphological evaluation of cross-sectional vessel shapes in hardwoods using image processing. Mokuzai Gakkaishi 43(9):709–716.

————, ————, AND M. FUJITA. 1999. Digital image analysis of cross-sectional tracheid shapes in Japanese softwoods using the circularity index and aspect ratio. J. Wood Sci. 45(2):98–105.

DONALDSON, L. A., AND M. J. F. LAUSBERG. 1998. Comparison of conventional transmitted light and confocal microscopy for measuring wood cell dimensions by image analysis. IAWA J. 19(3):319–334.

EVANS, R. 1994. Rapid measurement of the transverse dimensions of tracheids in radial wood selections from *Pinus radiata*. Holzforschung 48(2):168–172.

————, G. DOWNES, D. MENZ, AND S. STRINGER. 1995. Rapid measurement of variation in transverse dimensions in a radiata pine tree. Appita 48(2):134–138.

FUJITA, M., M. OHYMA, AND H. SAIKI. 1996. Characteris-ation of vessel distribution by Fourier Transform image analysis. Pages 36–44 in L. A. Donaldson, A. P. Singh, B. G. Butterfield, and L. J. Whitehouse, eds. Recent advances in wood anatomy. New Zealand Forest Research Institute Ltd.

GONZALEZ, R. F., AND R. E. WOODS. 1992. Digital image processing, Addison Wesley Publishing Co., Old Tapan, NJ. 716 pp.

HANNRUP, B., Ö. DANELL, I. EKBERG, AND M. MOËLL. 2001. Relationships between wood density and tracheid dimensions in Pinus sylvestris L. Wood Fiber Sci. 33(2): 173–181.

HOUGARDY, H. P. 1976. Recent progress in automatic image analysis instrumentation. Microscope 24:7–23.

ILIC, J., AND W. E. HILLIS. 1983. Video image processor for wood anatomical quantification, Holzforschung 37: 47–50.

JAGELS, R., AND M. W. DYER. 1983. Morphometric analysis applied to wood structure. I. Cross-sectional cell shape and area change in red spruce. Wood Fiber Sci. 15(4):376–386.

———. AND F. W. TELEWSKI. 1990. Computer-aided image analysis of tree rings. Pages 76–93 in L. Kairiukstis and E. Cook, eds. Methods of dendrochronology: Applications in the environmental sciences. Kluwer Academic Publishers, Dordrecht, The Netherlands.

JANG, H. F., A. G. ROBERTSON, AND R. S. SETH. 1992. Transverse dimensions of wood pulp fibres by confocal laser scanning microscopy and image analysis. J. Mater. Sci. 27:6391–6400.

KIBBLEWHITE, R. P. 1980. Radiata pine corewood and slab-wood, and their interrelations with pulp and handsheet properties basic densities and tracheid lengths. N.Z. Forestry Sci. 10(3):533–550.

———. 1999. Designer fibres for improved papers through exploiting genetic variation in wood micro-structure. Pages 469–477 in Proc. 53rd Appit Annual Conference, 19–23 April. Rotorua, New Zealand, (PA-PRO Report No. B252).

LEE J., AND D. ROSEN. 1985. On the use of automated microscopy in wood research. Holzforschung 39:1–6.

MCMILLIN, C. W. 1982. Application of automatic image analysis to wood science. Wood Science 14(3):97–105.

MOËLL, M., AND G. BORGEFORS. 1998. A machine-vision method to measure cross-sectional tracheid dimensions of wood using confocal microscopy. Pages 216–221 in Proc. Image Vision and Computing New Zealand, November 16–18, Auckland, New Zealand.

ORBERT, C. L., E. W. BENGTSSON, AND B. G. NORDIN. 1993. Watershed segmentation of binary images using distance transformations. Pages 159–170 in Proc. Image Processing: Nonlinear Image Processing IV SPIE 1902. 31 January–5 February, San José, CA.

PAPE, R., B. PERSSON, E. STÅHL, and M. MOËLL. 2001. Influence of thinning on cross-sectional tracheid dimensions in Norway spruce. Wood Fiber Sci. (submitted).

PARK, W.-K., AND F. W. TELEWSKI. 1993. Measuring maximum latewood density by image analysis at the cellular level. Wood Fiber Sci. 25(4):326–332.

PEACHEY, T. C., AND C. F. OSBORNE. 1990. The measurement of wood cell parameters using the distance transform. Wood Fiber Sci. 22(4):388–403.

RANEFALL, P., K. WESTER, AND E. BENGTSSON. 1998. Automatic quantification of immunohistochemically stained cell nuclei using unsupervised image analysis. Analyt. Cellular Pathol. 16(1):29–43.

SANNITI DI BAJA, G. 1994. Well-shaped, stable and reversible skeletons from the (3,4)-distance transform. J. Visual Comm. and Image Represent. 5(1):107–115.

SCHALER, S. M., L. H. GROOM, AND L. MOTT. 1996. Microscopic analysis of wood fibers using environmental scanning electron microscopy and confocal microscopy. Pages 25–32 in Proc. Wood-fibre-Plastic Composites Symp. Forest Prod. Soc., Madison, WI.

SCHNELL, G. R., AND J. SELL. 1989. Bildanalytische Messung des Zellwandantels bzw. der Dichte von Holz-Präparationsmethode, Messtechnik. Holz Roh- Werkst. 47: 351–354.

TELEWSKI, F. W., A. H. WAKEFIELD, AND M. J. JAFFE. 1983. Computer-assisted image analysis of tissues of ethrel-treated Pinus taeda seedlings. Plant Physiol. 72:177–181.

VINCENT, L., AND P. SOILLE. 1991. Watersheds in digital spaces: An efficient algorithm based on immersion simulations. IEEE Trans. Pattern Analysis and Machine Intelligence 13(6):583–598.

YANOSKY, T. M., AND C. J. ROBINOVE, 1986. Digital image measurement of the area and anatomical structure of tree rings. Can. J. Botany 64(12):2896–2902.

YU, B., AND A. K. JAIN. 1996. A robust and fast skew detection algorithm for generic documents. Pattern Recognition 29(10):1599–1629.